

## Supporting Information for

# Back-propagating rupture evolution within a curved slab during the 2019 Peru intraslab earthquake

Yaping Hu<sup>\*, a</sup>, Yuji Yagi<sup>b</sup>, Ryo Okuwaki<sup>b, c, d</sup>, Kousuke Shimizu<sup>a</sup>

<sup>a</sup> Graduate School of Life and Environmental Sciences, University of Tsukuba, Ibaraki 305-8572, Japan

<sup>b</sup> Faculty of Life and Environmental Sciences, University of Tsukuba, Ibaraki 305-8572, Japan

<sup>c</sup> Mountain Science Center, University of Tsukuba, Ibaraki 305-8572, Japan

<sup>d</sup> COMET, School of Earth and Environment, University of Leeds, Leeds LS2 9JT, UK

## Contents

- Figure S1: Finite-fault inversion results for different maximum rupture front velocity
- Figure S2: Waveform fitting for the finite-fault inversion
- Figure S3: Snapshots of N1 nodal plane in 2 s steps from 20 s to 40 s
- Figure S4: Synthetic test results
- Figure S5: Snapshots of synthetic test
- Figure S6: Comparison between developed and conventional inversion
- Figure S7: Slip distribution on a length-extended model plane

## Supplementary text

Text S1: Synthetic test

We performed a synthetic test to evaluate the robustness of the waveform inversion result and the resolvability of the T-axis azimuth rotation. Here, the preferred source model of the 2019 Peru earthquake was adopted as the input source model (Fig. 3c). We used the same initial rupture point and stations as were used in the waveform inversion (Fig. 2). For the calculation of synthetic waveforms, we added Green's function and background noise errors. For the Green's function error, random Gaussian noise with a mean of zero and a standard deviation of 2% of the maximum amplitude of each calculated Green's function was added. For the background noise error, we added random Gaussian noise with a mean of zero and a standard deviation of 1  $\mu\text{m}$  to the synthetic waveforms. In our inversion, the input synthetic data were resampled every 0.8 s without applying any filter to either the theoretical Green's functions or the input waveform. The synthetic waveforms could well explain the input waveforms. The focal mechanisms of the output model were consistent with those of the input model in the main rupture area (Fig. S4a). With regard to the total slip distribution, the major rupture was observed from 30 km south to 200 km north of the hypocenter

\* Corresponding Author  
[yaping-hu@geol.tsukuba.ac.jp](mailto:yaping-hu@geol.tsukuba.ac.jp) (Yaping Hu)

in the output model; this distribution well reproduces the input model (Fig. S4a). The synthetic test snapshots (Fig. S5) show that the initial rupture propagated eastward and downdip (0 to 15 s). The main rupture subsequently propagated northward from the epicenter (15 to 30 s), then bilaterally both northward and southward (30 to 45 s), and finally unilaterally northward (45 to 80 s). The rupture process of the synthetic test was reconstructed from the finite-fault inversion results. In addition, the clockwise rotation of the T-axis azimuths in the output model (Fig. S4b) from south to north of the epicenter was consistent with the rotation of the T-axis azimuths in the input model (Fig. 3e). We therefore consider the flexible source model of the 2019 Peru earthquake to be valid for resolving both the rupture complexity and the variation of the fault geometry (T-axis azimuth distribution) of the 2019 Peru earthquake.

#### Text S2: Verification of the highly flexible source model

In this study, we applied a newly developed finite-fault inversion method (Shimizu et al., 2020) to mitigate the effects of modeling error originating from uncertainty of the fault geometry. We also applied the conventional finite-fault inversion method, assuming the same parameter settings as for the N1 fault plane, and evaluated how the modeling error of fault geometry affected the results. With both the new and conventional methods, the formulation of Yagi and Fukahata (2011) was employed in the same way to introduce the uncertainty of the Green's function into the data covariance matrix, and the hyperparameter that controls the strength of smoothing was determined by using Akaike's Bayesian Information Criterion (Akaike, 1980; Yabuki and Matsu'ura, 1992). By the conventional inversion, the seismic moment was inferred to be  $1.66 \times 10^{21}$  Nm ( $M_w$  8.1), which is comparable to the value of  $1.84 \times 10^{21}$  Nm ( $M_w$  8.1) inferred by using the newly developed inversion method. There was general agreement between the new and conventional results with regard to the location of the major slip area north of the hypocenter and the initial rupture area on the downdip side of the hypocenter (Figs. S6a, b). However, whereas the new flexible finite-fault inversion well reproduced the observed waveforms (Fig. S2), the conventional method could not reproduce the observed waveforms where the radiation pattern was sensitive to the assumed fault geometry (e.g., at stations RCBR and SHEL, Fig. S6c). With the conventional inversion method, the slip vectors gradually rotated clockwise from the hypocenter northward in the large-slip area; this rotation should partly reflect the clockwise T-axis azimuth rotation obtained by the new inversion result. The spatial resolution of our model was generally higher than that of the conventional model. The flexible representation of the fault deformation by the newly developed inversion method suppressed modeling errors originating from the uncertainty of fault geometry, resulting in a finer image (Fig. S6a) of the rupture process of the 2020 Peru earthquake.

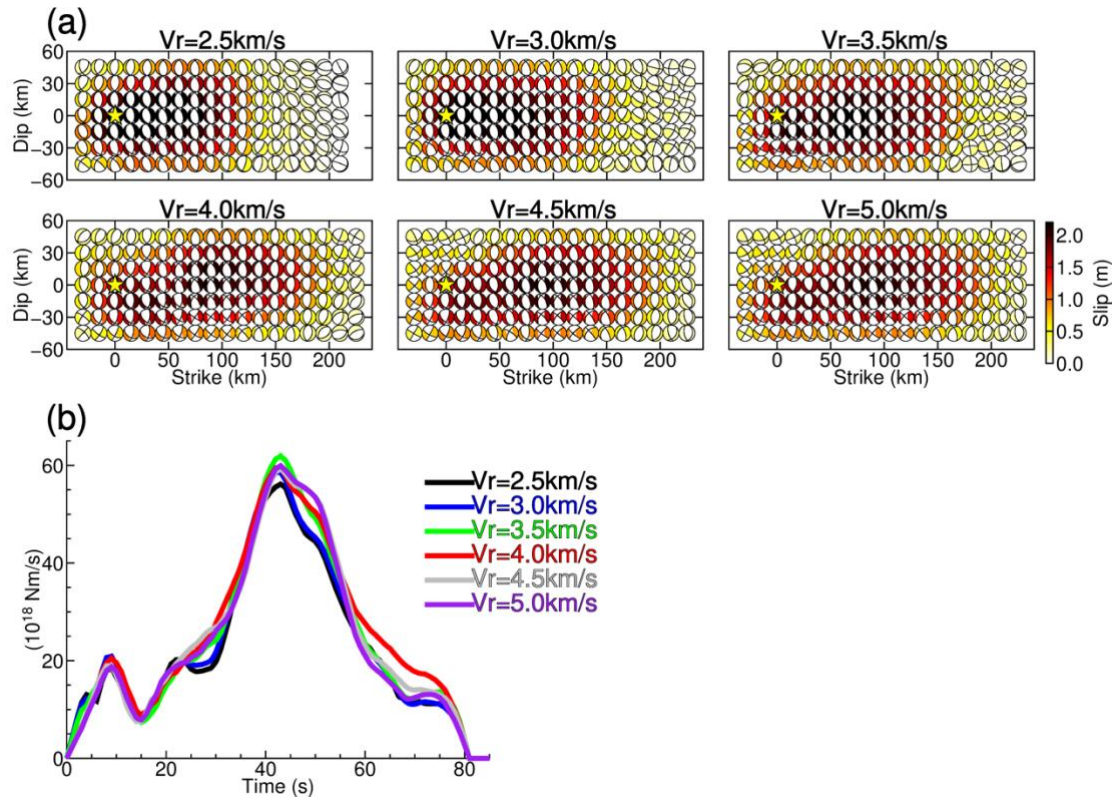
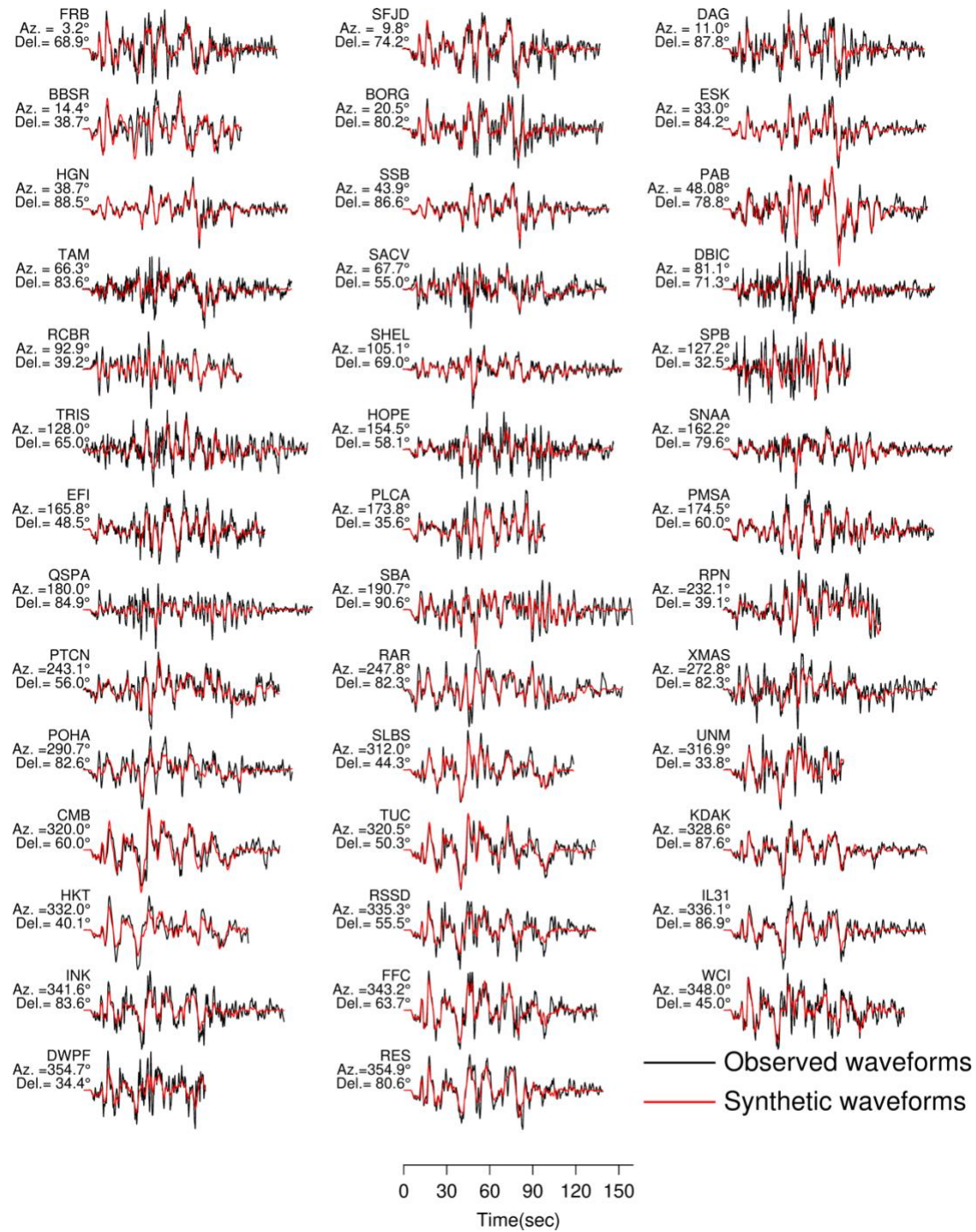


Figure S1: Finite-fault inversion results of different maximum rupture front velocity ranging from 2.5 to 5.0 km/s. (a) Spatial distribution of Focal mechanisms. The yellow stars show the hypocenter. (b) Moment rate function. Different color lines indicated moment rate function of different maximum rupture front velocity.



80

81

82 Figure S2: Waveform fitting between observed (black lines) and synthetic waveforms (red lines) produced by the  
 83 new flexible inversion method. Station code, azimuth and epicentral distance are shown on the right of each  
 84 waveform fitting.

85



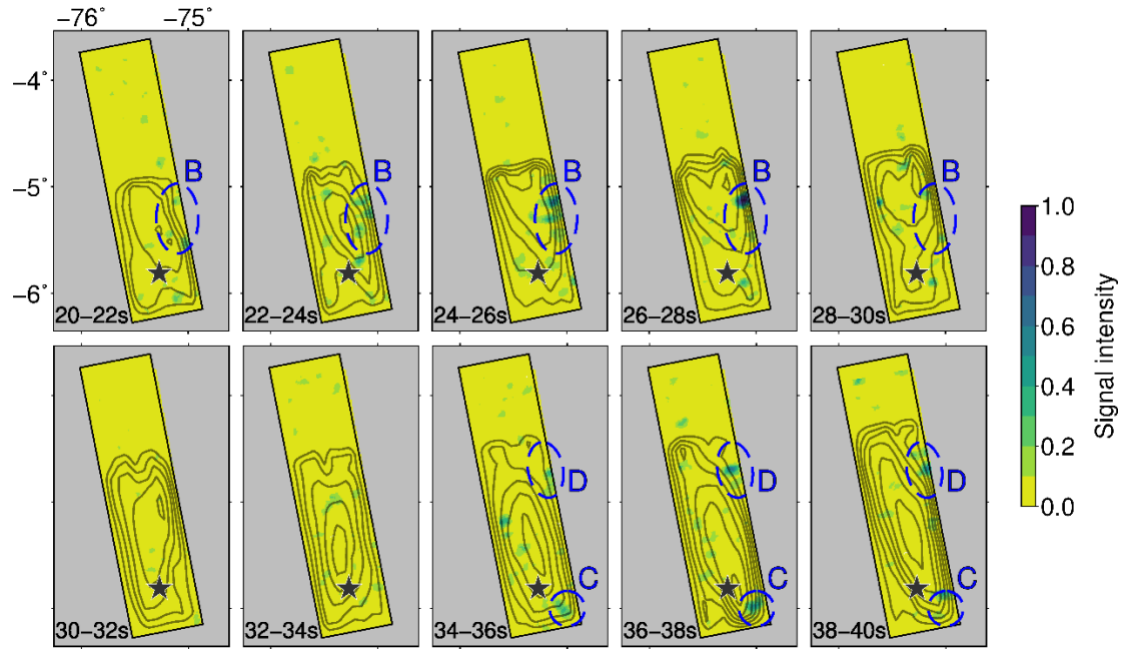


Figure S3: Snapshots of the distribution of average slip rate (contours) and normalized high-frequency radiation (color scale) at 2 s step from 20 s to 40 s. The black contour intervals of slip-rate are 0.02m/s.

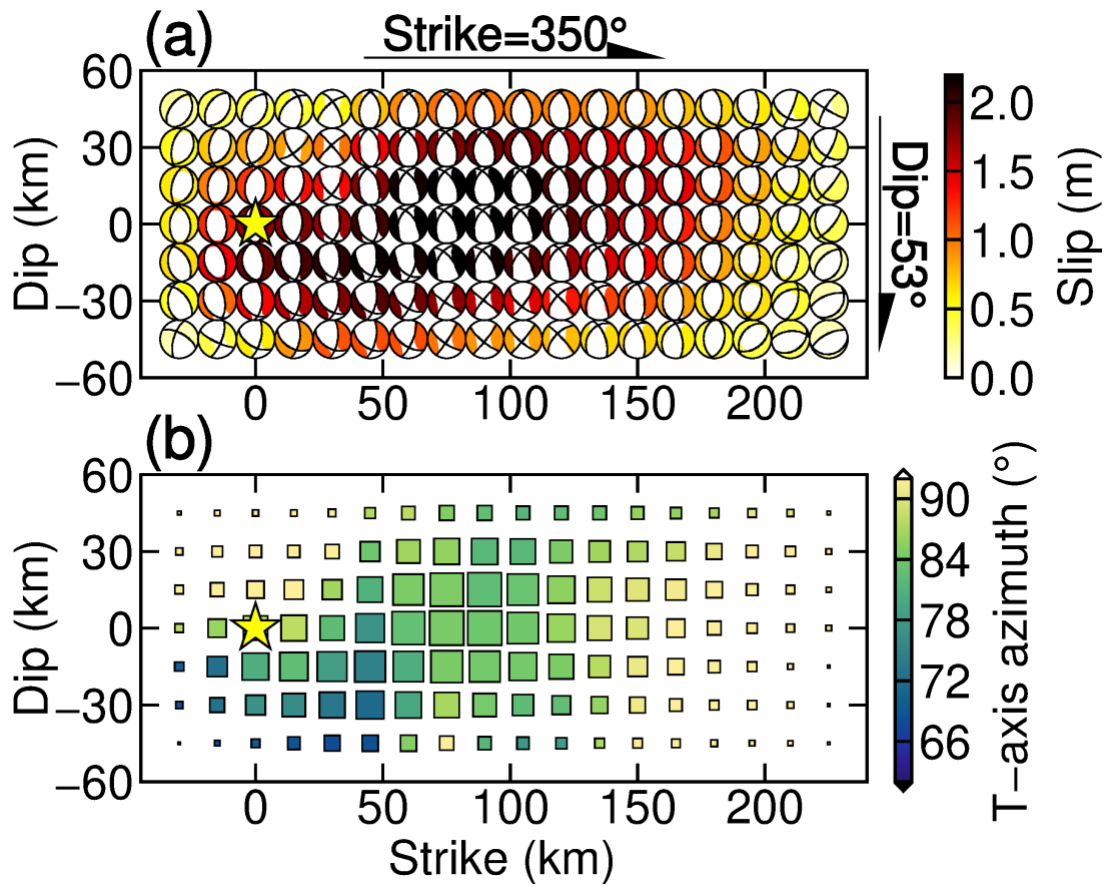
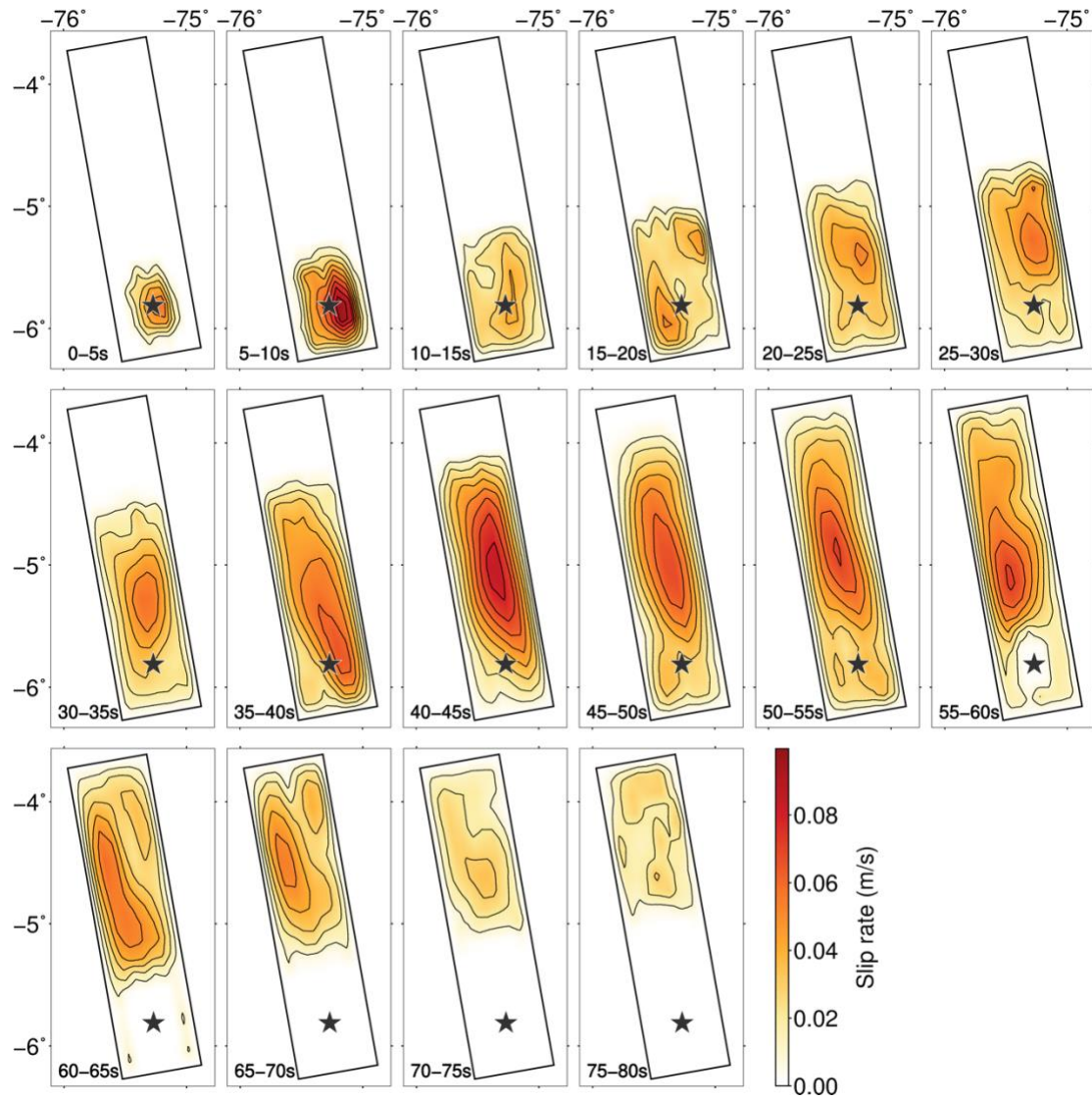


Figure S4: Synthetic test results. (a) Spatial distribution of the focal mechanisms. (b) The distribution of T-axis azimuth.

95



96

97

98 Figure S5: Snapshots of synthetic test at an interval of 5 s. The left bottom time is the time period of each snapshot

99 from the origin time. Black star shows the epicenter and black rectangle box shows the assumed fault plane. The

100 black contour intervals are 0.02m/s.

101

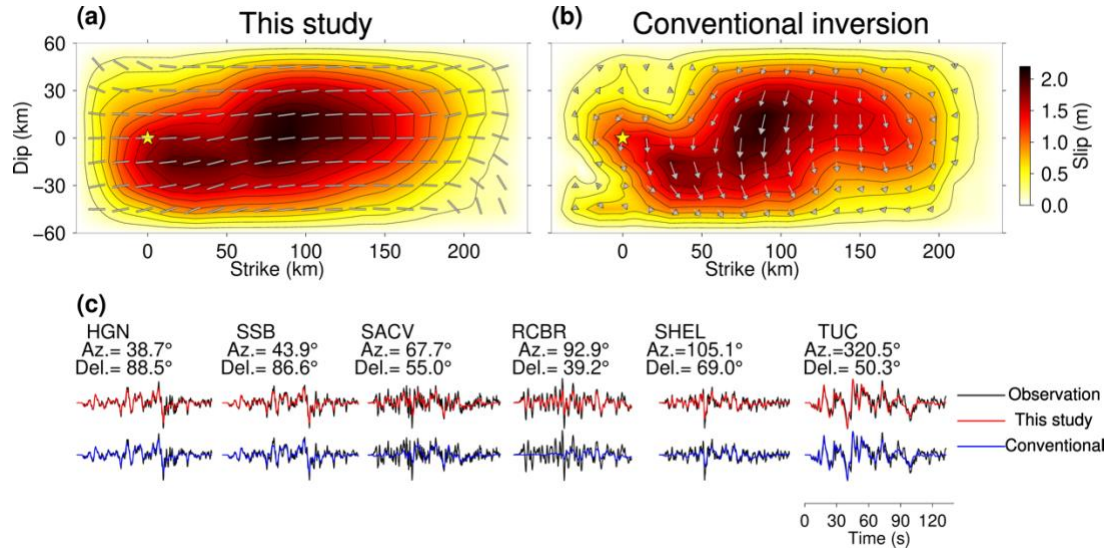


Figure S6: Comparison between the models obtained by applying developed and conventional inversion. (a) Slip distribution obtained by developed inversion. Black lines represent the T-axis azimuth distribution. (b) Slip distribution obtained by conventional inversion. Black arrows indicate the slip vectors. The black contour intervals are 0.02 m. Yellow stars indicate the hypocenter. (c) Comparison of waveform fitting for developed and conventional methods at selected stations.

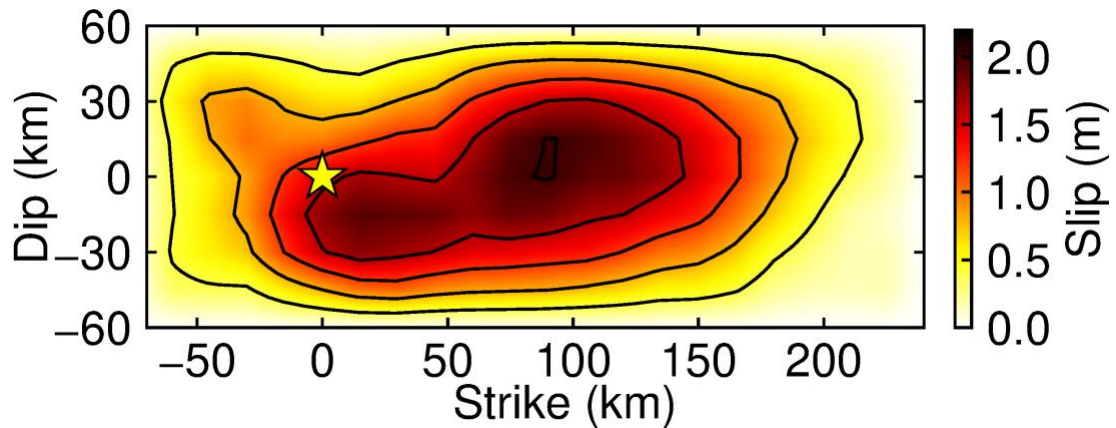


Figure S7: Slip distribution on a length-extended model plane. The interval of slip is 0.4m.

## Reference

- Akaike, H., 1980. Likelihood and the Bayes procedure, *Trabajos de Estadística Y de Investigación Operativa*, 31(1), 143–166.
- Shimizu, K., Yagi, Y., Okuwaki, R. Fukahata, Y., 2020. Development of an inversion method to extract information on fault geometry from teleseismic data, *Geophys. J. Int.*, 220 (2), 1055–1065, doi: [10.1093/gji/ggz496](https://doi.org/10.1093/gji/ggz496).
- Yabuki, T. & Matsu'ura, M., 1992. Geodetic data inversion using a Bayesian information criterion for spatial distribution of fault slip, *Geophys. J. Int.*, 109(2), 363–375, doi: [10.1111/j.1365-246X.1992.tb00102.x](https://doi.org/10.1111/j.1365-246X.1992.tb00102.x).

121 Yagi, Y. & Fukahata, Y., 2011. Introduction of uncertainty of Green's function into waveform inversion for seismic  
122 source processes, *Geophys. J. Int.*, 186(2), 711–720, doi: [10.1111/j.1365-246X.2011.05043.x](https://doi.org/10.1111/j.1365-246X.2011.05043.x).  
123